Paper No.
7657

NACE INTERNATIONAL CORROSION 2016 CONFERENCE & EXPO

Corrosion Behavior of Ultra-high Strength Drilling Steel in Alkaline Brines Containing Hydrogen Sulfide at High Temperature

Ruishu Feng, Justin R. Beck, Derek M. Hall, Ian Wolfe, Aysel Buyuksagis
and Serguei N. Lvov*
The EMS Energy Institute
Department of Energy and Mineral Engineering
Department of Materials Science and Engineering
The Pennsylvania State University, University Park, PA 16802, USA

Margaret Ziomek-Moroz*
U.S. Department of Energy
National Energy Technology Laboratory
1450 Queen Avenue SW, Albany, OR 97321, USA

*Corresponding authors: lvov@psu.edu
Margaret.Ziomek-Moroz@NETL.DOE.GOV

ABSTRACT

In-situ electrochemical measurements were used to study the sour corrosion of ultra-high strength low alloy carbon steel (UHSLA) in alkaline brines at 200 °C. The solutions were buffered with $NaHCO_3$ / Na_2CO_3 / NaOH to pH values calculated to be 8.1, 9.8, and 10.8 with the presence of H_2S gas at 200 °C. The partial pressure of H_2S was equivalent to 10 psi (69 kPa) at 85 °C. According to thermodynamic calculations, the dominant reactive ion changed from HCO_3^-(aq) to OH^-(aq) with a comparable concentration of HS^-(aq) as pH increased. Measured polarization resistance values at 200 °C were one to two orders of magnitude lower than those at 85 °C, which corresponded to a drastic increase in corrosion rate. After 60 hours, the corrosion rates (CR) were 0.84 mm y^{-1}, 2.88 mm y^{-1}, and 1.83 mm y^{-1} from pH 8.1 to 10.8. The CR calculated with commercial software was in reasonable agreement with the experimental CR. Limiting current was observed in the anodic region using linear sweep voltammetry (LSV) but not in the cathodic region. Even with the effect of limiting current, anodic Tafel slopes, b_a, were able to be gathered from LSV using a new method derived from the generalized Butler-Volmer equation. The b_a values indicated that the anodic reactions followed the Bockris mechanism at pH 8.1 and a two-electron mechanism at pH 9.8 and 10.8. Cathodic Tafel slopes corresponded to a two-electron mechanism in the three conditions. Two layers were observed on the surface at pH 8.1 and 9.8, and the outer layer spalled off in some regions. As the pH increased, the major corrosion products transitioned from pyrrhotite/siderite to magnetite, and the S distribution moved outward from the inner layer.

Keywords: Sour corrosion; H_2S gas; High strength carbon steel; High temperature; Alkaline brines; Electrochemical corrosion; Corrosion scales characterization.

©2016 by NACE International.
Requests for permission to publish this manuscript in any form, in part or in whole, must be in writing to
NACE International, Publications Division, 15835 Park Ten Place, Houston, Texas 77084.
The material presented and the views expressed in this paper are solely those of the author(s) and are not necessarily endorsed by the Association.

INTRODUCTION

Carbon steel has been widely used for deep drilling in oil and gas industry due to its high strength:weight ratio and economical cost. However, with the presence of H_2S, carbon steel has been found to be more susceptible to hydrogen induced cracking (HIC) / sulfide stress cracking (SSC), which would lead to catastrophic failure and drastic cost increase during the exploration.[1,2]

Sour corrosion has been extensively studied from many perspectives, which can generally be categorized to the reaction mechanism with the presence of H_2S and the effect of corrosion scales.[3–8] A solid state reaction was proposed between Fe and H_2S to form mackinawite in unstirred saturated aqueous H_2S solutions at 21 °C and atmospheric pressure.[9] The corrosion rate and protectiveness of corrosion products were influenced by pH, H_2S concentration, and immersion time.[10] The rate determining step changed from diffusion control to interfacial reaction control when H_2S concentration increased.[11,12] Most of the studies were conducted from pH 3 to 8 at a mild temperature from 20 to 95 °C.

However, typically a drilling fluid of pH 10 to 12 flowing through the drilling pipe is used to increase the pH in practice, and the temperature in deep wells can reach above 200 °C. Therefore, the drilling steel is exposed to a neutral to basic environment containing corrosive substances such as H_2S, CO_2, and brine at high pressure and high temperature. Corrosion of carbon steel in H_2S-containing deaerated alkaline brines has been studied previously by the authors at 85 °C.[13–15] The corrosion rate was found to decrease as pH increased from 7.9 to 12.4 at low H_2S partial pressure ($P_{H2S} \leq 0.12$ psi or 0.83 kPa), whereas the CR was the fastest at the intermediate pH of 10.7 when P_{H2S} increased to 1.2 psi (8.3 kPa) and 10 psi (69 kPa). It was proposed that the diversity of reactive ions in the solutions and the non-homogeneity of the corrosion scale could have triggered an increase in localized corrosion at the intermediate pH. Further study was conducted to determine if the trend would continue at 200 °C in this work.

Corrosion studies at high temperature often encounter challenges due to the limitation of the equipment material and difficult handling and control. Ramanarayanan and Smith reported that diffusion of Fe^{2+} through a growing pyrrhotite film was the rate-limiting step in H_2S-saturated, brine condition at 204 °C.[16] In alkaline brines at 200 °C, the effects of high pH and high temperature on the corrosion rate and corrosion scale were studied in the present work to understand the sour corrosion mechanism in drilling fluid conditions. The generalized Bulter-Volmer equation was employed to analyze LSV data to study the reaction mechanisms.

EXPERIMENTAL

Materials

UHSLA steel, a proprietary modification from UNS G41300, was investigated. Its chemical composition is listed in Table 1.[17]

Table 1: Chemical composition (%wt.) of UHSLA[17]

Fe	Cr	Mn	Mo	Al	Ni	Cu	Nb	Si
Bal	0.79	0.88	0.67	0.03	0.81	0.19	0.02	0.26
S	**P**	**B**	**C**	**N**	**V**	**Sn**	**Ti**	
0.007	<0.005	<0.005	0.27	0.007	0.07	<0.01	<0.01	

©2016 by NACE International.
Requests for permission to publish this manuscript in any form, in part or in whole, must be in writing to
NACE International, Publications Division, 15835 Park Ten Place, Houston, Texas 77084.
The material presented and the views expressed in this paper are solely those of the author(s) and are not necessarily endorsed by the Association.

Steel samples were machined into 10×20×5 mm plate electrodes which were coated with epoxy so that only one 10×20 mm face was exposed the corrosive solutions. The exposed surface was ground by 600 and 800 grit SiC papers and then polished by 0.05 micron alumina polishing solution to minimize the surface defects and keep the surface area as consistent as possible. The polished steel sample was rinsed with propanol and distilled water and then wiped dry. Heat shrinkable polytetrafluoroethylene (PTFE) tubing was used to coat the electrode leads attached to the steel samples.

System Setup

A three-electrode system was adopted in a deaerated autoclave to carry out the electrochemical measurements. The working electrode was the prepared steel sample. The counter electrode was a 10×20×1 mm platinum plate which was also coated with epoxy. The leads were coated with PTFE tubing the same way as the steel samples. The two electrodes were held in place with the polished surfaces parallel to each other with a distance of 10 mm between them.

A double-junction silver-silver chloride (Ag/AgCl) electrode was prepared inside a ceramic tube to be the reference electrode to prevent the contamination from the test solutions. The reference electrode was filled with 5 %wt. NaCl(aq) solution to minimize the concentration gradient, and thus the junction potential, between the reference and test solutions. The Ag/AgCl reference electrode potential was calculated with Gibbs energy minimization to be 61 mV±12 mV vs SHE at 200 ^{o}C using thermodynamic values from literature and then with values from a commercial database.[18]

The reactor vessel was a 600 mL autoclave constructed of stainless steel UNS S31600. A schematic diagram of the autoclave system is shown in Figure 1.[15] The system temperature was controlled and recorded through a controller connected to a heating mantle. A computer-controlled potentiostat was used to perform in-situ electrochemical measurements.

Experimental Procedure

The test solutions contained 5 %wt. (0.9 mol kg^{-1}) NaCl and were buffered with different concentrations of $NaHCO_3$, Na_2CO_3, and NaOH. The solution compositions are listed in Table 2. All of the solutions were prepared in 250 g deionized water and then deaerated by Ar for at least one hour. The sealed autoclave was purged of oxygen with Ar as well. The deaerated solution was transferred to the autoclave through a plastic dip tube (No. 6 in Figure 1) by the pressure difference while Ar was flushing. After the system was heated up to 85 °C, a H_2S/N_2 mixture gas (10%vol. H_2S) was introduced into the autoclave through the plastic tube until P_{H2S} reached 10 psi (69 kPa). This way the total amount of H_2S in the system was constant over the test and comparable to the previous tests at 85 ^{o}C. Using the ideal gas law and the vapor volume in the reactor vessel (236.3 mL), the total H_2S concentration was estimated to be 2.19 × 10^{-2} mol kg^{-1}.[13] Ar gas was added to increase the total pressure to 265 psi (1.83 MPa). Then all of the valves were closed. The autoclave was further heated up to 200 °C. The total pressure went up to around 505 psi (3.48 MPa) due to the increased temperature and water vaporization, and then kept steady around 475 psi (3.28 MPa) over the course of corrosion. The solution pH at 200 ^{o}C with this amount of H_2S was computed using commercial software and is given in Table 2.[19] The pH calculation was set to take into account system pressure, temperature, and the components inside the autoclave. The addition of H_2S slightly decreased the pH due to the dissociation of H_2S. The pH in the same solution compositions at 85 ^{o}C were 7.7, 10.5, and 12.4 from Solution #1 to #3, respectively.[14] The solution pH was altered due to a larger ionization constant of H_2O(l) at 200 ^{o}C and different dissociation constants of the components.

©2016 by NACE International.
Requests for permission to publish this manuscript in any form, in part or in whole, must be in writing to
NACE International, Publications Division, 15835 Park Ten Place, Houston, Texas 77084.
The material presented and the views expressed in this paper are solely those of the author(s) and are not necessarily endorsed by the Association.

Linear polarization resistance (LPR), electrochemical frequency modulation (EFM), and electrochemical impedance spectroscopy (EIS) measurements were performed every two hours over the exposure period with the stir rate of 525 RPM. LPR was carried out over the potential range of ±10 mV with respect to the corrosion potential (E_{corr}), and the sweep rate was 1 mV s^{-1}. EFM was operated at the base frequency of 0.01 Hz with the multipliers of 2 and 5, and the amplitude was 20 mV with respect to E_{corr}.[20] EIS was measured over the frequency range of 300 kHz to 5 mHz with the amplitude of 10 mV. After 60 hours, LSV was carried out with the sweep rate of 5 mV s^{-1} from -200 mV to +200 mV vs E_{corr}. After the electrochemical corrosion tests, the corroded surfaces were examined using scanning electron microscopy (SEM), energy dispersive X-ray spectroscopy (EDS), and X-ray diffraction (XRD).

Table 2: Solution compositions (mol kg^{-1}) and pH at 200 °C

Soln.	NaCl	$NaHCO_3$	Na_2CO_3	NaOH	pH, no H_2S	pH with H_2S
1	0.9	0.5	0	0	8.2	8.1
2	0.9	0	1	0	9.9	9.8
3	0.9	0	1	1	10.8	10.8

Calculation of the Corrosion Rate

In a three-electrode cell, when the corrosion is under the charge transfer control / activation control and the working electrode is polarized within a sufficiently small region around E_{corr}, the corrosion current density, $j_{corr,}$ can be calculated according to the Stern-Geary equation as shown in Equations (1) and (2).[21,22]

$$j_{corr} = 1/ (R_{ct}\, B') = 1/ (R_{pol}\, B') \quad (1)$$

$$B' = (\ln 10)\, (b_c + b_a) / (b_c\, b_a) \quad (2)$$

where R_{ct} is the area-specific charge transfer resistance, which is equal to R_{pol}, the area-specific polarization resistance, when corrosion is under the charge transfer control. B' is a combination of the cathodic, b_c, and anodic, b_a, Tafel slopes. R_{pol} can be obtained from the slope around E_{corr} in the LPR plot after correction for the solution resistance. The Tafel slopes can be obtained from real-time EFM. The corrosion rate (CR), defined as the depth of corrosion penetration per time, can be calculated following Equation (3).

$$CR = j_{corr}\, M / (nF\rho) \quad (3)$$

where M is the molecular mass of the corroding metal, n is the electron number, F is the Faraday constant (96485 C mol^{-1}), and ρ is the metal density.

The Stern-Geary equation is the application of the Butler-Volmer equation in corrosion when both anodic and cathodic reactions are under charge transfer control. However, when one of the reactions, anodic or cathodic, is limited by a non-electrochemical step like mass transport at E_{corr}, the Stern-Geary equation is no longer applicable. The generalized Butler-Volmer equation with terms of limiting current density has to be introduced to derive the relations between overpotential and current density. For a corrosion system, the generalized Butler-Volmer equation can be written in Equations (4) to (5), assuming that current densities from the reduction direction of anodic process and the oxidation direction of cathodic process are negligible. [23,24]

©2016 by NACE International.
Requests for permission to publish this manuscript in any form, in part or in whole, must be in writing to
NACE International, Publications Division, 15835 Park Ten Place, Houston, Texas 77084.
The material presented and the views expressed in this paper are solely those of the author(s) and are not necessarily endorsed by the Association.

$$j = j_{\mathrm{corr}}\left[\left(1-\frac{j}{j_{\mathrm{lim,a}}}\right)\exp\left(\frac{\eta}{B_{\mathrm{a}}}\right)-\left(1-\frac{j}{j_{\mathrm{lim,c}}}\right)\exp\left(-\frac{\eta}{B_{\mathrm{c}}}\right)\right] \quad (4)$$

$$B_{\mathrm{a}} = b_{\mathrm{a}} / \ln 10,\ B_{\mathrm{c}} = b_{\mathrm{c}} / \ln 10 \quad (5)$$

where j is the current density, η the overpotential vs E_{corr}, $j_{\mathrm{lim,a}}$ the anodic limiting current density, $j_{\mathrm{lim,c}}$ the cathodic limiting current density. B_{a} is the anodic Tafel parameter, and B_{c} is the cathodic Tafel parameter.

Assuming only the anodic reaction is affected by a limiting current, $j_{\mathrm{lim,c}}$ is an infinite value and Equation (4) becomes Equation (6).

$$j = j_{\mathrm{corr}}\left[\left(1-\frac{j}{j_{\mathrm{lim,a}}}\right)\exp\left(\frac{\eta}{B_{\mathrm{a}}}\right)-\exp\left(-\frac{\eta}{B_{\mathrm{c}}}\right)\right] \quad (6)$$

Two scenarios are discussed here. Scenario one is when η is very large in the anodic region and the cathodic contribution is insignificant. Then Equation (6) becomes Equation (7) or (8). Equation (8) allows us to obtain the Tafel slope b_{a} as the slope of η-$\log_{10}[j/(j_{\mathrm{lim,a}}-j)]$ when the LSV plot is complicated by a limiting current.[23]

$$j = j_{\mathrm{corr}}\left[\left(1-\frac{j}{j_{\mathrm{lim,a}}}\right)\exp\left(\frac{\eta}{B_{\mathrm{a}}}\right)\right] \quad (7)$$

or

$$\eta = B_{\mathrm{a}}\ln\left(\frac{j_{\mathrm{lim,a}}}{j_{\mathrm{corr}}}\right)+B_{\mathrm{a}}\ln\left(\frac{j}{j_{\mathrm{lim,a}}-j}\right) = b_{\mathrm{a}}\log_{10}\left(\frac{j_{\mathrm{lim,a}}}{j_{\mathrm{corr}}}\right)+b_{\mathrm{a}}\log_{10}\left(\frac{j}{j_{\mathrm{lim,a}}-j}\right) \quad (8)$$

Scenario two is when η is very large in the cathodic region and the anodic contribution is insignificant. It will be a normal Tafel plot expressed as in Equation (9).

$$\eta = B_{\mathrm{c}}\ln(j_{\mathrm{corr}}) - B_{\mathrm{c}}\ln(-j) = b_{\mathrm{c}}\log_{10}(j_{\mathrm{corr}}) - b_{\mathrm{c}}\log_{10}\ln(-j) \quad (9)$$

RESULTS AND DISCUSSION

Primary Species in the Solutions

The speciation in each solution with H_2S was calculated using commercial software.[19] Figure 2 shows the primary carbonate and sulfide species at 200 °C with the H_2S concentration of 2.19×10^{-2} mol kg^{-1}. As pH increased from 8.1 to 10.8, the concentrations of hydrogen-containing species decreased, such as H_2CO_3(aq), HCO_3^-(aq), and H_2S(aq), whereas the concentrations of CO_3^{2-}(aq) and S^{2-}(aq) increased. HS^-(aq) concentration had a small fluctuation as pH increased. Note that H_2CO_3(aq) was represented by CO_2(aq) in this paper assuming that Gibbs energy of CO_2(aq)+H_2O(l)=H_2CO_3(aq) reaction is zero. Comparing to the similar conditions at 85 °C from the authors' previous work,[14] the speciation trend with pH of carbonate and sulfide species were similar; however, the concentration of each species changed at 200 °C due to the differences in water ionization constant and dissociation constants, resulting in different pH values.

It has been proposed by different researchers that OH^-(aq), HCO_3^-(aq), and HS^-(aq) could be the reactive ions for the anodic reactions of Fe dissolution, and that H_2O(l), H^+(aq) and H_2S(aq) for hydrogen evolution reaction (HER) at the cathodic side. [9,10,25,26] The concentrations of these

©2016 by NACE International.
Requests for permission to publish this manuscript in any form, in part or in whole, must be in writing to
NACE International, Publications Division, 15835 Park Ten Place, Houston, Texas 77084.
The material presented and the views expressed in this paper are solely those of the author(s) and are not necessarily endorsed by the Association.

reactive species are listed in Table 3. The concentrations of H^+(aq) and H_2S(aq) decreased from Solution #1 to #3. The dominant reactive ion for the anodic reactions generally changed from HCO_3^-(aq) to OH^-(aq) with a similar concentration of HS^-(aq) from Solution #1 to #3. Solution #2 had the most diverse reactive ions with comparable concentrations of these three ions.

Table 3: The concentrations of primary reactive species in the three solutions (mol kg^{-1})

Solution	# 1	# 2	# 3
H^+(aq)	1.02E-08	1.51E-10	1.28E-11
H_2S(aq)	5.11E-04	1.44E-05	1.86E-06
OH^-(aq)	1.56E-03	9.66E-02	9.08E-01
HCO_3^-(aq)	4.12E-01	1.30E-01	1.04E-02
HS^-(aq)	2.08E-02	2.11E-02	1.78E-02

Polarization Resistance and Corrosion Rate

Figures 3 shows R_{pol} and CR of the UHSLA steel changing with time in the three solutions at 200 °C with b_{H2S} = 2.19×10^{-2} mol kg^{-1}. R_{pol} gradually increased in Solutions #1 and #3 before 60 hours, whereas R_{pol} first increased and then decreased during the first 36 hours in Solution #2. The increase of R_{pol} could be related to the formation of corrosion products and the decrease of reactive area on the surface. The decrease of R_{pol} could be related to the corrosion products spalling from the surface or the increased occurrence of localized corrosion. R_{pol} was approaching the steady state after 60 hours in all the three solutions. R_{pol} at steady state was the smallest in Solution #2.

CR followed the inverse trend of the R_{pol}. In Solutions #1 and #3, CR gradually decreased with time. In Solution #2, CR decreased and then increased during the first 36 hours, and then slightly decreased until 60 hours. Due to the drastic increase of CR following the initial decrease, CR in Solution #2 was the highest at steady state, 2.88 mm y^{-1}. CR in Solutions #1 and #3 were relatively slower with the values of 0.84 and 1.83 mm y^{-1}, respectively. Interestingly, CR in the three solutions were within in a factor of 4, while there was at least one order of magnitude difference for the same conditions at 85 °C.[13,15] Moreover, R_{pol} decreased by factors of 20, 12, and 70 from Solution #1 to #3 at 200 °C compared with 85 °C. Inversely, the corrosion rates were significantly accelerated at 200 °C.

The experimental CR at steady state was compared with CR calculated using commercial modeling software in Figure 4. The hydrodynamic model was based on the rotating disk electrode. The corrosion rates were predicted to be 4.77, 0.157, and 0.833 mm y^{-1}, respectively. The modeled CR was higher at pH 8.1, and lower at pH 9.8 and 10.8. Despite the divergence, the modeling results were in reasonable agreement with the experimental CR.

Linear Sweep Voltammetry Results

LSV plots were corrected for solution resistance and are depicted in Figure 5 (left). A limiting current density (j_{lim}) was observed on the anodic polarization region, and j_{lim} became smaller as pH increased from Solution #1 to #3. Mass transport, passivation, or a non-faradaic chemical step were all possible to cause limiting current density. Firstly, the mass transport includes the diffusion and convection of reactants or products in the bulk solution or the pore solution within the corrosion scales.[27] Secondly, passivation occurs when a protective film is covering the surface. Since the current density did not drop radically, there was either a non-fully covered film or ions/vacancies still being able to pass through the passive film. The former one would still maintain

©2016 by NACE International.
Requests for permission to publish this manuscript in any form, in part or in whole, must be in writing to
NACE International, Publications Division, 15835 Park Ten Place, Houston, Texas 77084.
The material presented and the views expressed in this paper are solely those of the author(s) and are not necessarily endorsed by the Association.

the feature of active corrosion only with a smaller current density magnitude, therefore, it is unlikely to be this case. The latter one is the mass transport of ions/vacancies through the lattice of a solid film. The transport of Fe^{2+} ion through the iron sulfide film proposed by Ramanarayanan and Smith can be seen as this case. [16] The transport of Fe^{2+} vacancy from the film/solution interface toward the metal/film interface would also be plausible.[28] Here we expanded the concept of mass transport from the commonly accepted diffusion/convection in the aqueous phase to include the transport through the lattice of solid film. Thirdly, the chemical step could be the adsorption of OH^-(aq), HCO_3^-(aq), and HS^-(aq) forming intermediates with Fe.[9,10,25,26] However, the adsorption of charged ions usually has a potential dependence, which would not cause a plateau in current density. Thus, mass transport in the solution or through the lattice of the solid film is more likely to be the limiting step.

A peak was observed in the three solutions when the steel sample was positively polarized by ~200 mV, which might be the further oxidization of Fe(II) to Fe(III), and then the current was limited again. Another peak was observed at a smaller positive polarization (~50 mV) in Solutions #1 and #2 but not in Solution #3. This peak frequently appeared in H_2S-containing systems in the authors' previous study, which might correspond to the sulfide-related reaction.

Because of the anodic limiting current densities, anodic Tafel slopes were obtained using the slope in E-$\log_{10}[j/(j_{lim,a}-j)]$ plots as shown in Figure 5 (right). This method was derived from the behavior predicted in Equation (8). The transformed plots for Solutions #2 and #3 showed good linear regions and ba values are given in Table 4. However, the plot in Solution #1 at the stir rate of 525 RPM was not showing an obvious linear region due to a relatively short range of limiting current between two peaks. Instead, the LSV result at 0 RPM was used for Figure 5 (right), which gave a b_a value of 0.066 V dec^{-1}. On closer inspection, there was actually a short linear region before the limiting current in the LSV plot for Solution #1 in Figure 5 (left). This region gave a b_a value of 0.070 V dec^{-1}, which was very close, and the average of these two is listed in Table 4 as the anodic Tafel slope for Solution #1.

Table 4: Tafel slopes in the three solutions at 200 ºC after 60 hours.

Tafel slope / (V dec^{-1})	Solution # 1	Solution #2	Solution #3
b_a	0.068	0.098	0.085
b_c	0.105	0.117	0.095

Bockris et al proposed a mechanism of Fe dissolution as expressed in Reactions (10) to (12).[25] The rate determining step (RDS) is Step (II), the reduction of an intermediate FeOH(ad). Assuming the symmetry coefficient β to be 0.5, anodic Tafel slope of the Bockris mechanism was calculated to be 0.063 V dec^{-1} at 200 ºC according to Equation (13). b_a in Solution #1 was 0.068 V dec^{-1}, indicating that the Bockris mechanism could be the anodic mechanism in Solution #1. b_a values in Solutions #2 and #3 were very close to 0.094 V dec^{-1} which corresponded to a step of two electrons transferred simultaneously. The two-electron mechanism is written in a simplified form as shown in Reactions (14) and (15), and b_a was calculated according to Equation (16). OH^-(aq) could be substituted with HCO_3^-(aq) and HS^-(aq). The produced Fe^{2+} could further transport to the solution or deposit as corrosion scales on the steel surface. Note that Tafel slopes only illuminate the reaction mechanism without mass transport effect.

The Bockris mechanism:

Step I: $Fe(s) + OH^-(aq) \leftrightarrow FeOH(ad) + e^-$ (10)

Step II (RDS): $FeOH(ad) \rightarrow FeOH^+(aq) + e^-$ (11)

Step III: $FeOH^+(aq) + H^+(aq) \leftrightarrow Fe^{2+}(aq) + H_2O$ (12)

©2016 by NACE International.
Requests for permission to publish this manuscript in any form, in part or in whole, must be in writing to
NACE International, Publications Division, 15835 Park Ten Place, Houston, Texas 77084.
The material presented and the views expressed in this paper are solely those of the author(s) and are not necessarily endorsed by the Association.

$$b_a = 2.303\ (R\ T)/[(1+\beta)\ F] \quad (13)$$

where R is the gas constant (8.314 J K^{-1} mol^{-1}) and T the absolute temperature.

Two-electron mechanism for anodic reaction:

$$\text{Step I (RDS):} \quad Fe(s) \rightarrow Fe^{2+}(ad) + 2\ e^- \quad (14)$$

$$\text{Step II:} \quad Fe^{2+}(ad) \leftrightarrow Fe^{2+}(aq) \quad (15)$$

$$b_a = 2.303\ (R\ T)/(2\ \beta\ F) \quad (16)$$

In contrast, the cathodic region of the LSV plots showed a fairly linear region for Tafel analysis, and the cathodic Tafel slopes, b_c, are listed in Table 4. The linear region was observed to extend to more negative regions in cyclic voltammetry (CV) plots, which indicated that the Faradic behavior was not limited on the cathodic side. Considering the cathodic reaction occurred at the film/solution interface,[29] the hydrogen-containing species were sufficient because of effective stirring in the aqueous solution. For lack of H^+(aq) and H_2S(aq) in alkaline condition, H_2O(l) is considered to be the main reactant for HER.[30] Assuming the symmetry coefficient to be 0.5, cathodic Tafel slope of a two-electron reaction for HER was calculated to be 0.094 V dec^{-1}, which was close to b_c values in Table 4. Hydrogen-containing species were possibly ready to lose two-electrons simultaneously at 200 °C due to the promoted kinetics at high temperature. The two-electron mechanism is written in Equations (17) to (18). H_2O(l) could be substituted with H^+(aq) and H_2S(aq).[31]

Two-electron mechanism for cathodic reaction:

$$\text{Step I (RDS):} \quad 2\ H_2O(l) + 2\ e^- \rightarrow H_2(ad) + 2\ OH^-(aq) \quad (17)$$

$$\text{Step II:} \quad H_2(ad) \leftrightarrow H_2(g) \quad (18)$$

$$b_c = 2.303\ (R\ T)/(2\ \beta\ F) \quad (19)$$

Pourbaix Diagram

Figure 6 shows the Pourbaix diagram of Fe-H_2O-H_2CO_3-H_2S system in Solution #2 with H_2S concentration of 2.19×10^{-2} mol kg^{-1} at 200 °C. The Pourbaix diagrams in Solutions #1 and #3 are similar to in Solution #2. The thermodynamically predominant species changed from FeS(s)/FeS_2(s)/$FeCO_3$(s) to FeS(s)/Fe_3O_4(s) then to $HFeO_2^-$(aq) as pH changed from 8.1 to 9.8 then to 10.8.

Surface Analysis

The SEM images of corroded UHSLA steel surfaces are shown in Figure 7. Some representative EDS results are listed in Table 5 and the corresponding locations are marked on the SEM images. The EDS analysis was carried out at the accelerating voltage of 10 kV.

At 200 °C, the corrosion products were mixtures of iron carbonate, sulfide, and oxides in all of the three solutions; however, the morphology and elemental distribution varied. Two layers were observed on the steel surfaces at pH 8.1 and 9.8, and the outer layer partially stripped off from the steel. The EDS results at 8.1 showed that the Fe:S ratios were from 1:1 to 1:2 and the C:O ratios in Locations 1 and 4 were close to 1:3. Pyrrhotite ($Fe_{1-x}S$) and siderite ($FeCO_3$) were verified in the XRD pattern as shown in Figure 8. High O was detected on the surface at pH 9.8 and 10.8 and much lower S than at pH 8.1, which indicated that the majority of the corrosion products changed from iron sulfide to iron oxide as pH increased. Magnetite was determined by XRD to be the main corrosion scale at pH 9.8 and 10.8. At pH 10.8, the morphology was a film composed of

©2016 by NACE International.
Requests for permission to publish this manuscript in any form, in part or in whole, must be in writing to
NACE International, Publications Division, 15835 Park Ten Place, Houston, Texas 77084.
The material presented and the views expressed in this paper are solely those of the author(s) and are not necessarily endorsed by the Association.

mainly magnetite with some higher S-content particles on top of it. As the pH increased at 200 ^{o}C, the determined corrosion products changed from pyrrhotite/siderite to magnetite, which agreed with the prediction from Pourbaix diagram. During this transition, the corrosion scales at the intermediate pH of 9.8 could have been less protective, corresponding to the lowest R_{pol} measured from LPR. Another noteworthy observation was the distribution of S in the corrosion scales at different pH. S was higher in the inner layer than the outer layer at pH 8.1, whereas S was relatively higher in the outer layer at pH 9.8. At pH 10.8, S was higher in the particles on top of the film. The S distribution moved outward from the inner layer as pH increased.

Table 5: EDS chemical analyses in %at. on the corroded UHSLA steel surfaces in selected locations marked in Figure 7. (200 ^{o}C, b_{H2S} = 2.19 × 10^{-2} mol kg^{-1})

Location/pH	Fe	C	O	S	Na	Cl	Si
1 / 8.1	33	8.8	20	33	3.2	0.2	1.2
2 / 8.1	14	3.6	51	10	6.2	-	9.5
3 / 8.1	22	5.6	20	46	3.0	0.3	2.9
4 / 8.1	32	9.5	26	26	5.1	0.2	1.2
5 / 9.8	25	5.7	55	0.6	8.2	0.1	4.2
6 / 9.8	17	7.9	47	2.2	18	0.2	2.9
7 / 9.8	26	6.5	54	0.7	3.7	0.1	4.1
8 / 9.8	16	9.9	41	9.0	7.3	0.2	2.3
9 / 10.8	17	11	68	2.3	1.6	0.1	-
10 / 10.8	33	7.0	58	0.3	0.2	0.1	1.2
11 / 10.8	30	7.2	61	1.1	0.3	0.1	-
12 / 10.8	32	9.8	57	0.4	0.3	0.1	-

Considering OH^-(aq), HCO_3^-(aq), and HS^-(aq) as the reactants for anodic reactions, the competition of the surface coverage is influenced by the concentration and the nature of each ion like the structure and the specific adsorption. HCO_3^-(aq) ion has a larger size, so OH^-(aq) and HS^-(aq) could more easily occupy the inner Helmholtz plane on the steel surface than HCO_3^-(aq). Therefore, OH^-(aq) and HS^-(aq) could be more likely to form the inner layer. The variation of OH^-(aq):HS^-(aq) ratio corresponded to the major products in the inner layer being oxide or sulfide, which explained the pH dependence of S distribution in the corrosion scales according to the solution speciation in Table 3.

If anodic reactions take place at the metal/film interface and cathodic reactions at the film/solution interface, we could incorporate the corrosion scales with the electrochemical reaction mechanisms. According to LSV results, Fe could have formed intermediates with HS^-(aq), HCO_3^-(aq) or OH^-(aq) for anodic reactions at pH 8.1, while at pH 9.8 and 10.8 Fe could have lost two electrons simultaneously at the metal/film interface. The reasons for limiting current could be (a) the mass transport of the aqueous reactive ions or the produced Fe^{2+}(aq) through the porous layers, or (b) the diffusion of Fe^{2+} ion through the solid passive film. Further calculation of diffusion in aqueous phase and solid phase could be made to distinguish them.

CONCLUSIONS

Solution pH in the three solutions were calculated to be 8.1, 9.8, and 10.8 at 200 ^{o}C, respectively, which were 7.7, 10.5, and 12.4 at 85 ^{o}C for the same composition. The dominant reactive ion generally changed from HCO_3^-(aq) to OH^-(aq) with a comparable concentration of HS^-(aq) from Solution #1 to #3.

Polarization resistance values at 200 °C were consistently one to two orders of magnitude lower than at 85 °C, which corresponded to a drastic increase in corrosion rate at elevated

©2016 by NACE International.
Requests for permission to publish this manuscript in any form, in part or in whole, must be in writing to
NACE International, Publications Division, 15835 Park Ten Place, Houston, Texas 77084.
The material presented and the views expressed in this paper are solely those of the author(s) and are not necessarily endorsed by the Association.

temperature. At 200 °C, R_{pol} at 9.8 was the smallest after 60 hours among the three solutions. CR after 60 hours were 0.84 mm y^{-1}, 2.88 mm y^{-1}, and 1.83 mm y^{-1}, respectively, from pH 8.1 to 10.8. The modeled results were in reasonable agreement with the experimental CR values within a factor of 4.

A limiting current was observed in the anodic region of LSV but not in the cathodic region, which indicated that the anodic reactions were probably limited by the mass transport at 200 °C. Traditional Tafel analysis in the cathodic region gave cathodic Tafel slopes corresponding to a two-electron mechanism for the three solutions. A new method derived from the generalized Butler-Volmer equation allowed to obtain anodic Tafel slopes from LSV even with the effect of limiting current. The b_a values indicated that the anodic reactions followed the Bockris mechanism at pH 8.1 and a two-electron mechanism at pH 9.8 and 10.8.

Two layers of corrosion scales were observed on the surface at pH 8.1 and 9.8, and the outer layer spalled off in some regions. S was higher in the inner layer than the outer layer at pH 8.1, whereas S was relatively higher in the outer layer at pH 9.8. At pH 10.8, the morphology was a film with some higher S-content particles on it. As pH increased at 200 ºC, the major corrosion products changed from pyrrhotite/siderite to magnetite although the corrosion scales were a mixture of iron carbonate, sulfide and oxide. This trend was in accordance with the change of primary reactive ions and the Pourbaix diagram.

DISCLAIMER

This report was prepared as an account of work sponsored by an agency of the United States Government. Neither the United States Government nor any agency thereof, nor any of their employees, makes any warranty, express or implied, or assumes any legal liability or responsibility for the accuracy, completeness, or usefulness of any information, apparatus, product, or process disclosed, or represents that its use would not infringe privately owned rights. Reference herein to any specific commercial product, process, or service by trade name, trademark, manufacturer, or otherwise does not necessarily constitute or imply its endorsement, recommendation, or favoring by the United States Government or any agency thereof. The views and opinions of authors expressed herein do not necessarily state or reflect those of the United States Government or any agency thereof.

ACKNOWLEDGEMENTS

The authors would like to acknowledge Dr. Andre Anderko from OLI System Inc. for his helpful suggestions on the modeling with OLI Analyzer software and thank OLI Systems Inc. for providing access to the modeling software.

REFERENCES

1. M. Ziomek-Moroz, "Environmentally Assisted Cracking of Drill Pipes in Deep Drilling Oil and Natural Gas Wells," *J. Mater. Eng. Perform.* 21 (2012): p. 1061–1069.
2. R. S. Treseder, and T. M. Swanson, "Factors in Sulfide Corrosion Cracking of High Strength Steels," *CORROSION* 24 (1968): p. 31–37.
3. G. Zhang, *et al,* "Electrochemical corrosion behavior of carbon steel under dynamic high pressure H_2S/CO_2 environment," *Corros. Sci.* 65 (2012): p. 37–47.
4. J. B. Sardisco, W. B. Wright, and E. C. Greco, "Corrosion of Iron in an H_2S-CO_2-H_2O System: Corrosion Film Properties on Pure Iron," *CORROSION* 19 (1963): p. 354t–359t.
5. J. Tang, Y. Shao, T. Zhang, G. Meng, and F. Wang, "Corrosion behaviour of carbon steel in different concentrations of HCl solutions containing H_2S at 90°C," *Corros. Sci.* 53 (2011): p. 1715–1723.

©2016 by NACE International.
Requests for permission to publish this manuscript in any form, in part or in whole, must be in writing to
NACE International, Publications Division, 15835 Park Ten Place, Houston, Texas 77084.
The material presented and the views expressed in this paper are solely those of the author(s) and are not necessarily endorsed by the Association.

6. H. Vedage, T. A. Ramanarayanan, J. D. Mumford, and S. N. Smith, "Electrochemical Growth of Iron Sulfide Films in H_2S-Saturated Chloride Media," *CORROSION* 49 (1993): p. 114–121.
7. S. N. Smith, "Current Understanding of Corrosion Mechanisms Due to H_2S in Oil and Gas Production Environments," *CORROSION* 2015, paper No.5485.
8. K. Videm, and J. Kvarekvål, "Corrosion of Carbon Steel in Carbon Dioxide-Saturated Solutions Containing Small Amounts of Hydrogen Sulfide," *CORROSION* **51** (1995): p. 260–269.
9. D. W. Shoesmith, P. Taylor, M. G. Bailey, and D. G. Owen, "The Formation of Ferrous Monosulfide Polymorphs during the Corrosion of Iron by Aqueous Hydrogen Sulfide at 21°C," *J. Electrochem. Soc.* 127 (1980): p. 1007–1015.
10. H. Ma, "The influence of hydrogen sulfide on corrosion of iron under different conditions," *Corros. Sci.* 42 (2000): p. 1669–1683.
11. J. B. Sardisco, and R. E. Pitts, "Corrosion of Iron in an H_2S-CO_2-H_2O system, Mechanism of Sulfide Film Formation and Kinetics of Corrosion Reaction," *CORROSION* 21 (1965): p. 245–253.
12. J. B. Sardisco, and R. E. Pitts, "Corrosion of Iron in an H_2S-CO_2-H_2O System Composition and Protectiveness of the Sulfide Film as a Function of pH," *CORROSION* 21 (1965): p. 350–354.
13. R. Feng, J. R. Beck, R. Cianni, S. N. Lvov, and M. Ziomek-Moroz, "Corrosion of Carbon Steels in H_2S-Containing Alkaline Brines," *CORROSION* 2015, paper No. 6119.
14. R. Feng, *et al,* "Electrochemical Corrosion Behavior of High Strength Carbon Steel in H_2S-Containing Alkaline Brines," *ECS Trans.* 66 (2015): p. 13–36.
15. R. Feng, J. R. Beck, S. N. Lvov, and M. Ziomek-Moroz, "Effects of Hydrogen Sulfide on the Corrosion Behavior of High Strength Steel in Alkaline Solutions," *ECS Trans.* 61 (2014): p. 97–114.
16. T. A. Ramanarayanan, and S. N. Smith, "Corrosion of Iron in Gaseous Environments and in Gas-Saturated Aqueous Environments," *Corros. Sci.* 46 (1990): p. 66–74.
17. K. A. Rozman, "Corrosion and Fatigue of Oil Well Drilling Steels" (Master Thesis, Oregon State University, 2011).
18. D. M. Hall, N. N. Akinfiev, E. G. LaRow, R. S. Schatz, and S. N. Lvov, "Thermodynamics and Efficiency of a CuCl(aq)/HCl(aq) Electrolyzer," *Electrochim. Acta* 143 (2014): p. 70–82.
19. P. Wang, A. Anderko, and R. D. Young, "A speciation-based model for mixed-solvent electrolyte systems," *Fluid Phase Equilib.* 203 (2002): p. 141–176.
20. R. W. Bosch, J. Hubrecht, W. F. Bogaerts, and B. C. Syrett, "Electrochemical Frequency Modulation: A New Electrochemical Technique for Online Corrosion Monitoring," *CORROSION* 57 (2001): p. 60-70.
21. M. Stern, "A method for determining corrosion rates from linear polarization data," *CORROSION* 14 (1958): p. 60–64.
22. S. N. Lvov, *Introduction to Electrochemical Science and Engineering*. (CRC Press, 2015).
23. A. J. Bard, and L. R. Faulkner, *Electrochemical Methods: Fundamentals and Applications*. (2001).
24. D. Landolt, C*orrosion and Surface Chemistry of Metals*. (EPFL Press, 2007).
25. J. O. Bockris, D. Drazic, and A. R. Despic, "The Electrode Kinetics of the Deposition and Dissolution of Iron," *Electrochim. Acta* 4 (1961): p. 325–361.
26. J. Han, J. Zhang, and J. W. Carey, "Effect of bicarbonate on corrosion of carbon steel in CO_2 saturated brines," *Int. J. Greenh. Gas Control* 5 (2011): p. 1680–1683.
27. J. R. Park, and D. D. Macdonald, "Impedance studies of the growth of porous magnetite films on carbon steel in high temperature aqueous systems," *Corros. Sci.* 23 (1983): p. 295–315.
28. D. D. Macdonald, "The Point Defect Model for the Passive State," *J. Electrochem. Soc.* 139 (1992): p. 3434-3449.
29. G. A. Zhang, and Y. F. Cheng, "Localized corrosion of carbon steel in a CO_2-saturated oilfield formation water," *Electrochim. Acta* 56 (2011): p. 1676–1685.
30. M. Stern, "The Electrochemical Behavior, Including Hydrogen Over-voltage , of Iron in Acid Environments," *J. Electrochem. Soc.* 102 (1955): p. 609–612.
31. Y. Zheng, B. Brown, and S. Nešic, "Electrochemical Study and Modeling of H_2S Corrosion of Mild Steel," *CORROSION* 70 (2014): p. 351–365.

©2016 by NACE International.
Requests for permission to publish this manuscript in any form, in part or in whole, must be in writing to
NACE International, Publications Division, 15835 Park Ten Place, Houston, Texas 77084.
The material presented and the views expressed in this paper are solely those of the author(s) and are not necessarily endorsed by the Association.

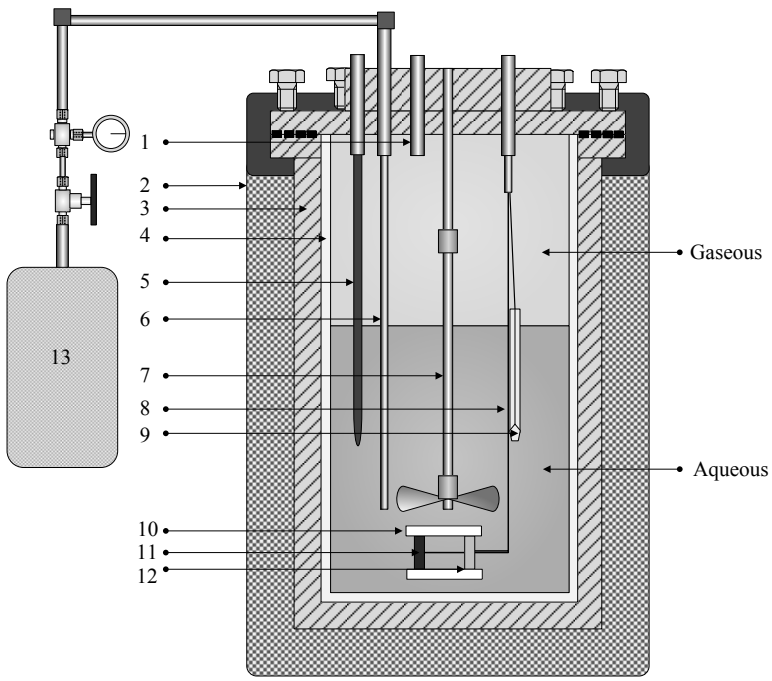

Figure 1: Schematic diagram of the autoclave system
1- Connection to pressure transducer; 2- Heating mantle; 3- Autoclave stainless steel vessel; 4- PTFE liner; 5- Polymer-coated thermocouple; 6- Plastic tubing; 7- Epoxy-coated stirrer; 8- PTFE-coated lead; 9- Ag/AgCl reference electrode; 10- PTFE assembly; 11- working electrode; 12- Pt counter electrode; 13- H_2S/N_2 cylinder.

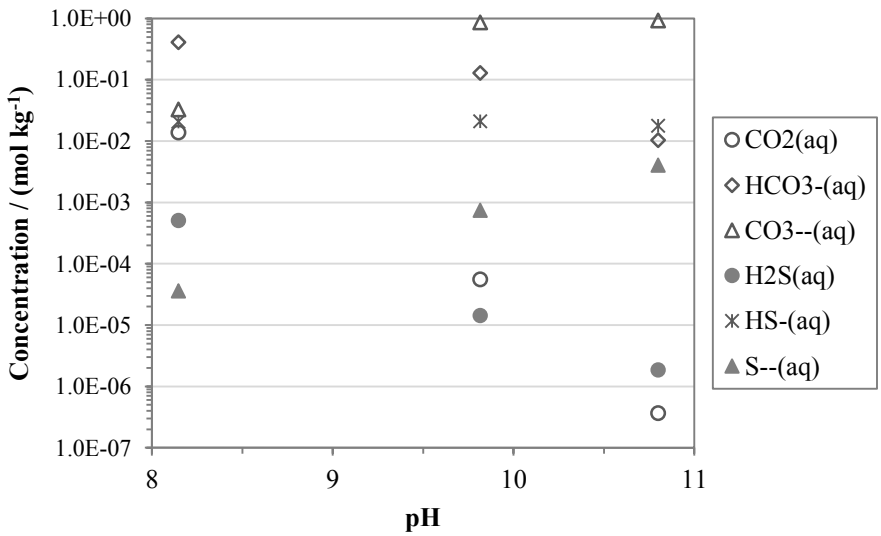

Figure 2: The primary carbonate and sulfide species in the three solutions at 200 °C with b_{H2S} = 2.19×10^{-2} mol kg^{-1}. (Solution #1: 0.9 mol kg^{-1} NaCl, 0.5 mol kg^{-1} $NaHCO_3$, pH = 8.1; Solution #2: 0.9 mol kg^{-1} NaCl, 1 mol kg^{-1} Na_2CO_3, pH = 9.8; Solution #3: 0.9 mol kg^{-1} NaCl, 1 mol kg^{-1} Na_2CO_3, 1 mol kg^{-1} NaOH, pH = 10.8).

©2016 by NACE International.
Requests for permission to publish this manuscript in any form, in part or in whole, must be in writing to
NACE International, Publications Division, 15835 Park Ten Place, Houston, Texas 77084.
The material presented and the views expressed in this paper are solely those of the author(s) and are not necessarily endorsed by the Association.

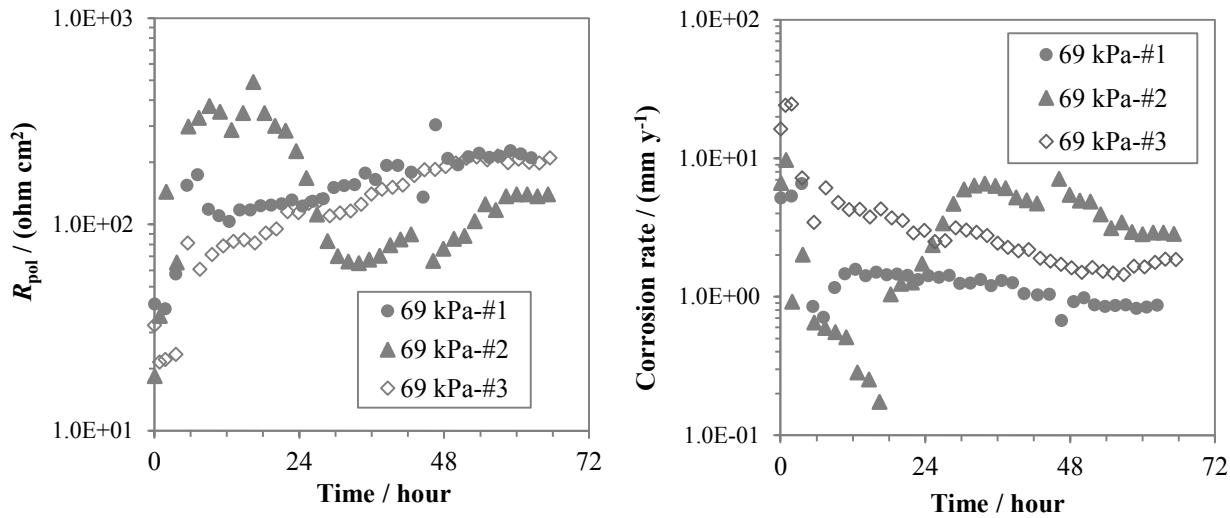

Figure 3: R_{pol} (left) and CR (right) of UHSLA changing with time in the three solutions at 200 ºC with b_{H2S} = 2.19×10^{-2} mol kg^{-1}. (Solution #1: 0.9 mol kg^{-1} NaCl, 0.5 mol kg^{-1} $NaHCO_3$, pH = 8.1; Solution #2: 0.9 mol kg^{-1} NaCl, 1 mol kg^{-1} Na_2CO_3, pH = 9.8; Solution #3: 0.9 mol kg^{-1} NaCl, 1 mol kg^{-1} Na_2CO_3, 1 mol kg^{-1} NaOH, pH = 10.8).

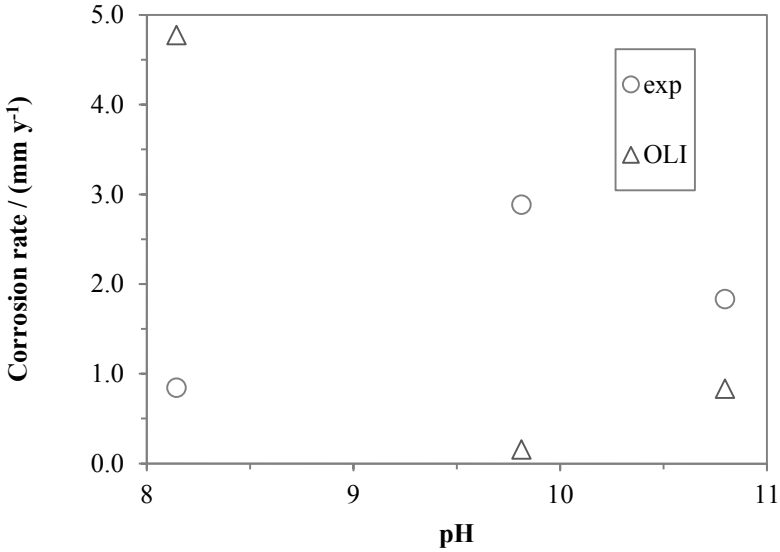

Figure 4: Experimental and modeled CR of UHSLA in the three solutions at 200 ºC with b_{H2S} = 2.19×10^{-2} mol kg^{-1}. (Solution #1: 0.9 mol kg^{-1} NaCl, 0.5 mol kg^{-1} $NaHCO_3$, pH = 8.1; Solution #2: 0.9 mol kg^{-1} NaCl, 1 mol kg^{-1} Na_2CO_3, pH = 9.8; Solution #3: 0.9 mol kg^{-1} NaCl, 1 mol kg^{-1} Na_2CO_3, 1 mol kg^{-1} NaOH, pH = 10.8).

©2016 by NACE International.
Requests for permission to publish this manuscript in any form, in part or in whole, must be in writing to
NACE International, Publications Division, 15835 Park Ten Place, Houston, Texas 77084.
The material presented and the views expressed in this paper are solely those of the author(s) and are not necessarily endorsed by the Association.

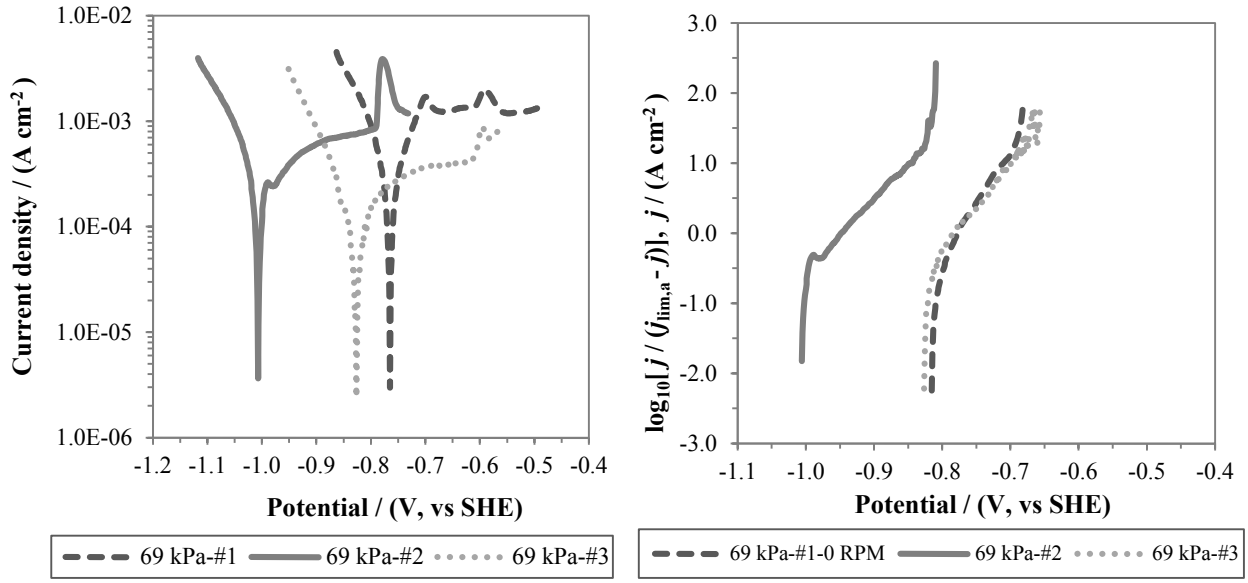

Figure 5: The LSV plots (left) and the transformed anodic LSV results (right) at 200 ºC with b_{H2S} = 2.19×10^{-2} mol kg^{-1} with the scan rate of 5 mV s^{-1}. Conditions: Stir rate of 525 RPM except for the one noted in the right figure. Solution #1: 0.9 mol kg^{-1} NaCl, 0.5 mol kg^{-1} $NaHCO_3$, pH = 8.1; Solution #2: 0.9 mol kg^{-1} NaCl, 1 mol kg^{-1} Na_2CO_3, pH = 9.8; Solution #3: 0.9 mol kg^{-1} NaCl, 1 mol kg^{-1} Na_2CO_3, 1 mol kg^{-1} NaOH, pH = 10.8.

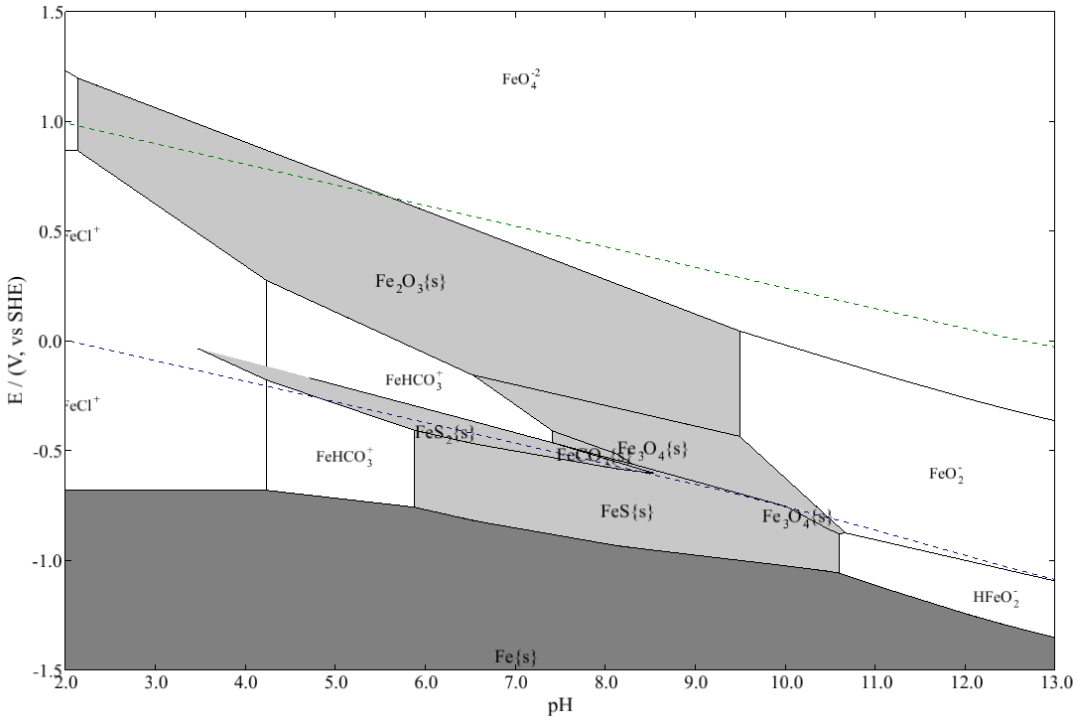

Figure 6: The Pourbaix diagram of Fe-H_2O-H_2CO_3-H_2S system in Soln. #2 with [H_2S] = 2.19 × 10^{-2} mol kg^{-1} at 200 ºC. (Soln. #2: 0.9 mol kg^{-1} NaCl, 1 mol kg^{-1} Na_2CO_3; Titrants: NaOH/HCl.)

©2016 by NACE International.
Requests for permission to publish this manuscript in any form, in part or in whole, must be in writing to
NACE International, Publications Division, 15835 Park Ten Place, Houston, Texas 77084.
The material presented and the views expressed in this paper are solely those of the author(s) and are not necessarily endorsed by the Association.

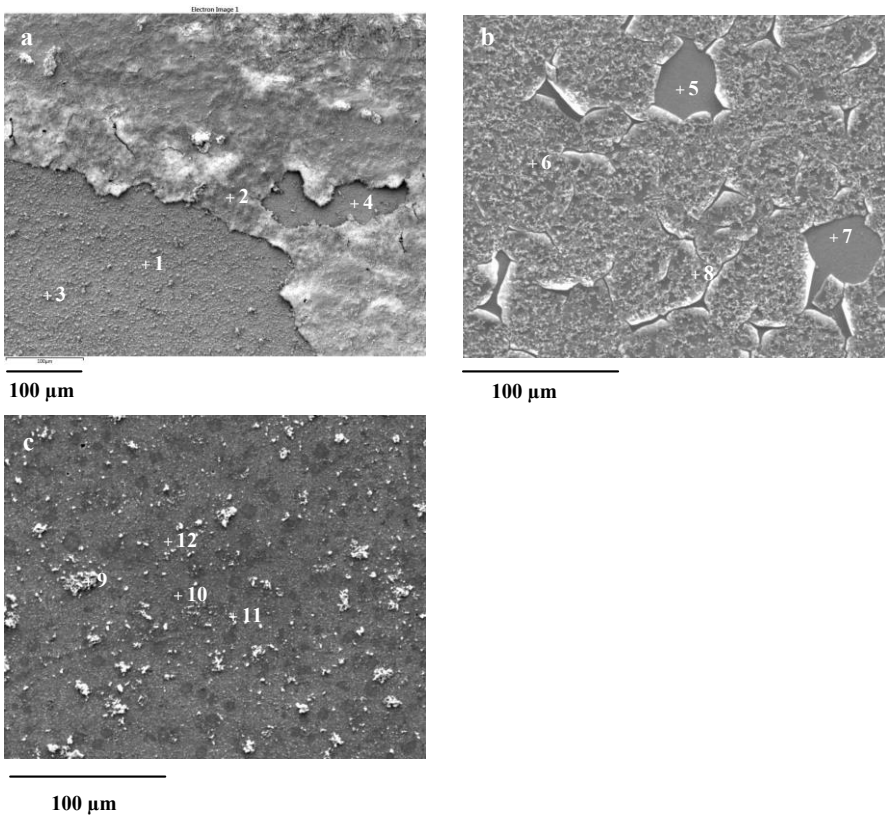

Figure 7: SEM images of the corroded UHSLA steel surfaces. Conditions: 200 °C, b_{H2S} = 2.19×10^{-2} mol kg^{-1}. Solution #1: 0.9 mol kg^{-1} NaCl, 0.5 mol kg^{-1} $NaHCO_3$, pH = 8.1; Solution #2: 0.9 mol kg^{-1} NaCl, 1 mol kg^{-1} Na_2CO_3, pH = 9.8; Solution #3: 0.9 mol kg^{-1} NaCl, 1 mol kg^{-1} Na_2CO_3, 1 mol kg^{-1} NaOH, pH = 10.8.

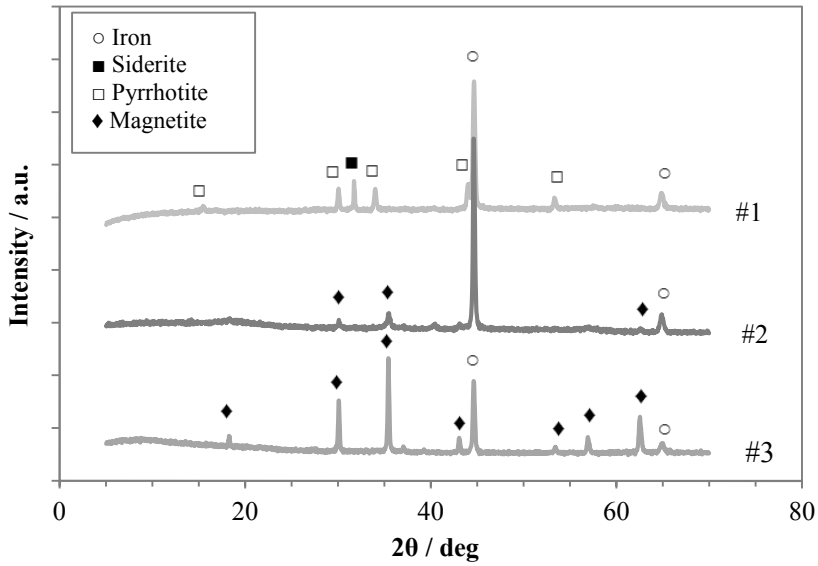

Figure 8: XRD results of corroded UHSLA surfaces in the three solutions with b_{H2S} = 2.19×10^{-2} mol kg^{-1} at 200 °C. Conditions: Solution #1: 0.9 mol kg^{-1} NaCl, 0.5 mol kg^{-1} $NaHCO_3$, pH = 8.1; Solution #2: 0.9 mol kg^{-1} NaCl, 1 mol kg^{-1} Na_2CO_3, pH = 9.8; Solution #3: 0.9 mol kg^{-1} NaCl, 1 mol kg^{-1} Na_2CO_3, 1 mol kg^{-1} NaOH, pH = 10.8.

©2016 by NACE International.
Requests for permission to publish this manuscript in any form, in part or in whole, must be in writing to
NACE International, Publications Division, 15835 Park Ten Place, Houston, Texas 77084.
The material presented and the views expressed in this paper are solely those of the author(s) and are not necessarily endorsed by the Association.